

Signal modeling of high-purity Ge detectors with a small read-out electrode and application to neutrinoless double beta decay search in ^{76}Ge

M. Agostini^{abcd*}, **C. A. Ur**^b, **D. Budjáš**^c, **E. Bellotti**^e, **R. Brugnera**^{bd},
C. M. Cattadori^e, **A. di Vacri**^f, **A. Garfagnini**^{bd}, **L. Pandola**^f, and **S. Schönert**^{ac}

^a Physikdepartment E15, Technischen Universität München, München, Germany

^b INFN Padova, Padova, Italy

^c Max-Planck-Institut für Kernphysik, Heidelberg, Germany

^d Dipartimento di Fisica dell'Università di Padova, Padova, Italy

^e INFN Milano Bicocca, Milano, Italy

^f INFN Laboratori Nazionali del Gran Sasso, Assergi, Italy

E-mail: matteo.agostini@ph.tum.de

ABSTRACT: The GERDA experiment searches for the neutrinoless double beta decay of ^{76}Ge using high-purity germanium detectors enriched in ^{76}Ge . The analysis of the signal time structure provides a powerful tool to identify neutrinoless double beta decay events and to discriminate them from gamma-ray induced backgrounds. Enhanced pulse shape discrimination capabilities of *Broad Energy Germanium* detectors with a small read-out electrode have been recently reported. This paper describes the full simulation of the response of such a detector, including the Monte Carlo modeling of radiation interaction and subsequent signal shape calculation. A pulse shape discrimination method based on the ratio between the maximum current signal amplitude and the event energy applied to the simulated data shows quantitative agreement with the experimental data acquired with calibration sources. The simulation has been used to study the survival probabilities of the decays which occur inside the detector volume and are difficult to assess experimentally. Such internal decay events are produced by the cosmogenic radio-isotopes ^{68}Ge and ^{60}Co and the neutrinoless double beta decay of ^{76}Ge . Fixing the experimental acceptance of the double escape peak of the 2.614 MeV photon to 90%, the estimated survival probabilities at $Q_{\beta\beta} = 2.039$ MeV are $(86 \pm 3)\%$ for ^{76}Ge neutrinoless double beta decays, $(4.5 \pm 0.3)\%$ for the ^{68}Ge daughter ^{68}Ga , and $(0.9^{+0.4}_{-0.2})\%$ for ^{60}Co decays.

KEYWORDS: Detector modeling and simulations, Particle identification methods, Gamma detectors.

*Corresponding author.

Contents

1. Introduction	1
2. Overview of the simulation	2
2.1 Field calculation, charge carrier transport and signal generation	3
2.2 Read-out electronics response and noise	5
3. Modeling of BEGe detectors	5
3.1 The electric field inside BEGe detectors	6
3.2 Signal development in dependence of the interaction position	7
3.3 Discrimination between single-site and multiple-site events	11
4. Validation of the simulation	12
4.1 The experimental setup	13
4.2 Pulse shape comparison with low energy gamma-ray beams	13
4.3 Rise time and A/E distributions studies	15
5. Background rejection and signal identification studies	20
5.1 Comparison of pulse shape discrimination of simulated and experimental data	20
5.2 Survival fractions of decays internal the Ge crystal	22
6. Conclusions and outlook	24

1. Introduction

The search for neutrinoless double beta decay ($0\nu\beta\beta$) is the only practical method to probe whether the neutrino is a Majorana particle, i.e. its own anti-particle. $0\nu\beta\beta$ decay violates lepton number conservation and would establish new physics beyond the Standard Model of particle physics. Provided that the exchange of light Majorana neutrinos are generating the leading term in $0\nu\beta\beta$ decay, effective neutrino masses down to a few tens of meV will be probed in the next generation of $0\nu\beta\beta$ decay experiments.

One promising isotope is ^{76}Ge . High-Purity Germanium (HPGe) detectors can be produced from germanium material enriched in ^{76}Ge , which serves simultaneously as a source and as detector medium. The advantages of the intrinsic radio-purity and excellent spectroscopic performance (2 – 3 keV full width at half maximum resolution at $Q_{\beta\beta} = 2039$ keV) of HPGe detectors have been recognized early [1], and until today, the most stringent experimental limits on $0\nu\beta\beta$ decay have been achieved with germanium crystals enriched in ^{76}Ge [2]. Also one group reported a claim of evidence [3].

The research work presented here was carried out in the framework of the GERmanium Detector Array (GERDA) experiment [4] which recently started its commissioning phase at the *Laboratori Nazionali del Gran Sasso* (LNGS) of the INFN in Italy. An array of bare HPGe detectors enriched to 86% in ^{76}Ge will be immersed in a cryogenic liquid which serves simultaneously as a coolant for the germanium detectors and as a high-purity shield against external radiation. The experiment pursues a staged implementation: the mentioned claim of evidence will be scrutinized in its first phase with about 15 kg · years exposure and a background index at $Q_{\beta\beta}$ of $< 10^{-2}$ counts/(keV · kg · year). The second phase of the experiment will explore half-lives up to $2 \cdot 10^{26}$ years, with 100 kg · years of exposure and background index of $< 10^{-3}$ counts/(keV · kg · year). Contingent on the results of the first two phases, a third phase is conceived to probe half-lives $> 10^{27}$ years. The corresponding effective neutrino mass of $\gtrsim 10$ meV is predicted based on the results of neutrino oscillation experiments assuming an inverted mass hierarchy [5]. To explore this parameter regime, an exposure of several 1000 kg · years and backgrounds $< 10^{-4}$ counts/(keV · kg · year) are required. To reach such background levels, which are about three orders of magnitude below the best current values, novel techniques are required which exploit the decay characteristics and topology of background events.

In recent works, we could show that p-type HPGe detectors produced by Canberra Semiconductor [6] with a small read-out electrode, referred to as thick-window *Broad Energy Germanium* (BEGe) detectors, exhibit pulse shape discrimination performance [7, 8] superior to coaxial HPGe detectors. This allows to efficiently distinguish between single-site events ($0\nu\beta\beta$ -like) and multi-site events (gamma-ray backgrounds). Investigations of a bare BEGe detector in liquid argon showed unaltered performance as compared to operation in a vacuum cryostat [9]. An additional benefit of the small size of the read-out electrode is its low capacitance which results into a lower noise and therefore a superior resolution and a lower threshold compared to other types of large-volume HPGe detectors. Following a full production chain test [10] of BEGe detectors with modified isotopic composition (depleted in ^{76}Ge), the GERDA collaboration decided to adopt thick-window BEGe detectors as their baseline design for the second phase of GERDA. R&D with BEGe detectors is also carried out by the Majorana collaboration [11, 12].

The scope of this paper is the ab-initio modeling of the signal pulse shapes of BEGe detectors created by particle interactions and the comparison with experimental data. The energy depositions and event topology were generated with the GEANT4 simulation package [13, 14] and the consequent signal pulse shape generated by drifting the charge carrier in the calculated electric field. The characteristic pulse shapes of the simulated pulses are then analyzed. First we validate the simulation of pulse shapes and discrimination methods with experimental data using calibration sources located externally to the crystal. Then, we calculate the expected pulse shape discrimination (PSD) cut efficiencies for ^{60}Co , ^{68}Ga and $0\nu\beta\beta$ decays internal to the detector. We also study the pulse shapes of energy depositions close to the small read-out electrode and in its vicinity.

2. Overview of the simulation

The simulation presented here replicates the physical processes involved in the generation of the Ge detector signals with application to the particular case of Broad Energy Germanium (BEGe) detectors. The simulation can be divided into three logical blocks: 1) interaction of ionizing par-

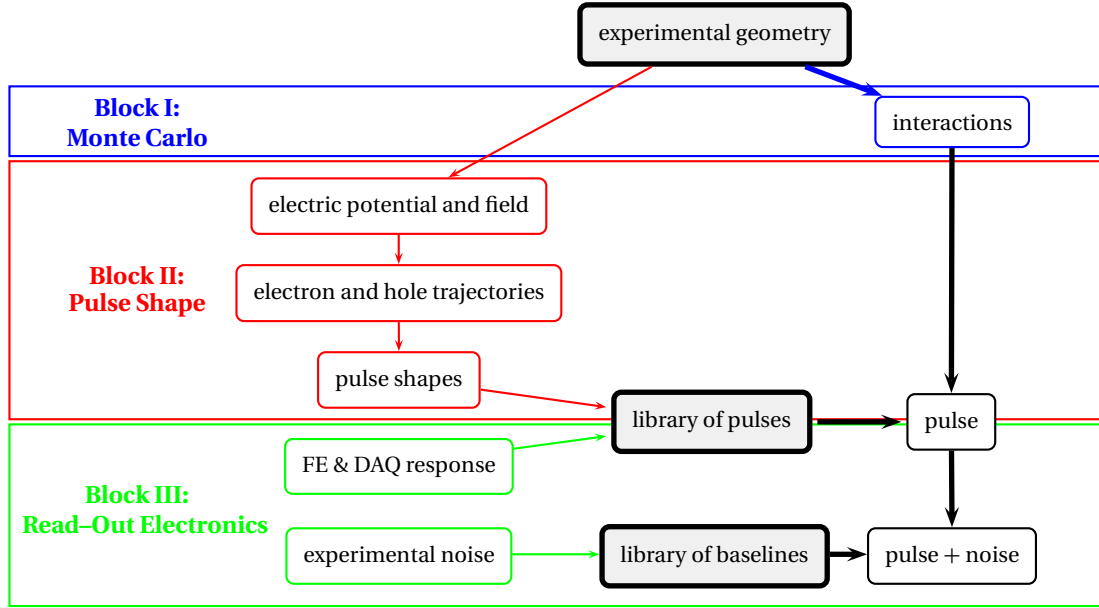


Figure 1. Data flow of the simulation organized into three logical blocks. The data flow includes a first phase (thin arrows) in which a library of pulses and baselines is created and a second phase (thick arrows) in which the libraries are used to generate the detector signals. In block III, FE & DAQ refers to the preamplifier and the sampling device.

ticles with the Ge crystal; 2) collection of the charge carriers produced at each interaction point at the detector electrodes and time evolution of the induced signals; 3) signal shaping by read-out electronic devices.

The first block consists of a Monte Carlo simulation, including all the physical processes involved in the passage of gamma-rays or charged particles through matter. It provides the interaction points and the corresponding energy losses within the crystal. This part of the simulation is performed within the MAGE framework [15], which is based on the GEANT4 simulation package [13, 14].

The second block describes the dynamics of the charge carriers generated inside the detector and provides the signals induced on the electrodes by the charge movement. It is calculated by using a modified version of the Multi Geometry Simulation (MGS) software [16].

The last block of the simulation takes into account the effects of the read-out electronic devices and of the electronic noise. It generates signals that can be directly compared to the measured ones.

Figure 1 illustrates the implementation diagram of these logical blocks in the software. In the following two subsections the second and the third block of the simulation are explained in more detail.

2.1 Field calculation, charge carrier transport and signal generation

The pulse simulation performed with the MGS-based software includes the following steps: 1) computation of the electric field inside the detector at defined potentials of the electrodes; 2) transport

of charge carries toward the electrodes; 3) time evolution of the signal induced at the read-out electrode by the moving charges.

Since a semiconductor detector can be considered as an electrostatic system, the electric field can be computed by solving the Maxwell equations or, equivalently, by solving the Poisson equation with a set of boundary conditions for the potential. In p-type Ge detectors, the p-n junction forms at the border of the ~ 1 mm thick donor-doped surface layer (n+ layer). At operational bias voltages the p-type volume is fully depleted of free charges (active volume), while most of the n+ layer retains electrons in the conduction band (anode, forming a dead layer). In our simulation we approximate this situation by defining the active volume with a negative space charge distribution ρ proportional to the net p-type impurity distribution, adjoined to the dead layer on which the bias voltage is applied¹. The boundary conditions are then provided by the value of the potential on the conductive surfaces: $V_{cathode}$ and V_{anode} . Therefore the system of equations to solve is:

$$\begin{cases} \nabla^2 \phi(\vec{r}) = -\rho(\vec{r})/(\epsilon_0 \epsilon_r) \\ \phi|_{S_{cathode}} = V_{cathode} \\ \phi|_{S_{anode}} = V_{anode} \end{cases} \quad (2.1)$$

where \vec{r} is the position, $\phi(\vec{r})$ is the electric potential, $\rho(\vec{r})$ is the charge density distribution, ϵ_0 is the vacuum electrical permittivity, $\epsilon_r \sim 16$ is the relative permittivity of Ge, $\phi|_S$ is the potential at the surface S surrounding the considered electrode.

The movement of charge carriers within the active volume is computed by using two phenomenological models [17, 18] which provide the drift velocity as a function of the electric field magnitude and of the electric field direction relative to the crystallographic axes. We assume that each transfer of energy to the Ge crystal lattice results in the generation of a cloud of free electrons and holes, which further drift as two independent clusters. These are approximated in our simulation by two point-like charges with opposite sign. The trajectories are calculated with a fourth order Runge-Kutta method with 1 ns time step.

Using the simulated trajectories of charge carriers and the weighting potential² distribution inside the detector, the charge signal $Q(\vec{r}(t))$ induced on the electrodes is computed by using the Shockley-Ramo theorem [19]:

$$Q(\vec{r}(t)) = -q_{tot} \phi_w(\vec{r}(t)) \quad (2.2)$$

where $\vec{r}(t)$ is the position of the charge cluster at the time t , q_{tot} the total charge of the cluster and $\phi_w(\vec{r}(t))$ is the weighting potential.

The total signal of a simulated particle event composed of several interactions is calculated as a sum of pulses from each hit, whose position and energy deposition are provided beforehand with the MAGE Monte Carlo simulation. To reduce the computation time, the generation of the signals corresponding to the individual hits is performed by using a library of pre-calculated pulses. The library is generated by dividing the detector active volume in 1 mm^3 cubic cells, and simulating

¹Since our field calculation is performed on a 0.5 mm step grid, it can not describe the thin part of the n+ volume in which the conduction-band electrons are depleted (the n-side of the p-n junction, with positive space charge).

²The *weighting potential* is a dimension-less quantity defined as the electric potential calculated when the considered electrode is kept at a unit potential, all other electrodes are grounded and all charges inside the device are removed.

a single normalized interaction at each corner. The library must be generated only once for each simulated detector geometry and bias voltage setting. Then each Monte Carlo generated interaction is associated to one of the cubic cells in the pulse library. The signal is computed as the weighted average of the eight pulses in each corner of the cube, where the weight is given by the inverse of the cubic euclidean distance between the interaction point and the considered corner. The amplitudes of the individual interaction pulses are then normalized according to the energy depositions in the hits and all the pulses of the event are added up to one combined signal.

The use of a pulse library decreases significantly the processing time of the simulation in such a way that the pulse computation time is comparable with that of the Monte Carlo simulation.

2.2 Read-out electronics response and noise

The read-out electronics includes the preamplifier and the digital sampling device. The response function was determined by providing the preamplifier input with an impulse generated by a high-precision pulser, and then by deconvolving the digitally sampled signal with the input signal. The simulated detector signals are consequently convolved with this response function. This is performed for each pulse in the library mentioned in previous subsection, so that it needs to be done only once for each simulated experimental setup.

To reproduce the electronic noise present in the experimental data, samples are taken from a library of experimentally recorded baselines. The amplitude of the noise is normalized according to the experimental signal-to-noise ratio, and the noise sample is then added to the calculated full event signal. The output of the simulation is a file of signals similar to those recorded experimentally with a digital data acquisition system. Therefore it is possible to apply the same analysis tools to both experimental and simulated data.

3. Modeling of BEGe detectors

The detector used for the present simulation is a modified thick-window version of a *Broad Energy Germanium* (BEGe) detector [20], a standard p-type High-Purity Ge (HPGe) detector offered by Canberra Semiconductor. These detectors have a cylindrical shape and a small B-implanted p+ electrode on one of the flat surfaces. The Li-infused n+ electrode (between 0.4 mm and 0.8 mm in the “thick window” modification) covers the rest of the outer surface and is separated from the p+ electrode by a circular groove. The detector is mounted in a 1.5 mm thick cylindrical aluminum housing. The positive high voltage is applied to the n+ electrode while the signal is read out from the p+ electrode where the holes are collected. For the purpose of the present work the specific case of the BE3830/S model was considered. The BE3830/S model has a diameter of 71 mm and a thickness of 32 mm. The detector was experimentally characterized in Refs. [21, 22]. A schematic drawing of a typical BEGe detector is shown in Figure 2.

In this section the signal formation and development in the BEGe detectors will be discussed following the steps outlined in Section 2.1. Moreover, the results of the simulation will be used to show how it is possible to distinguish between single-site and multiple-site events by analyzing the pulse shapes.

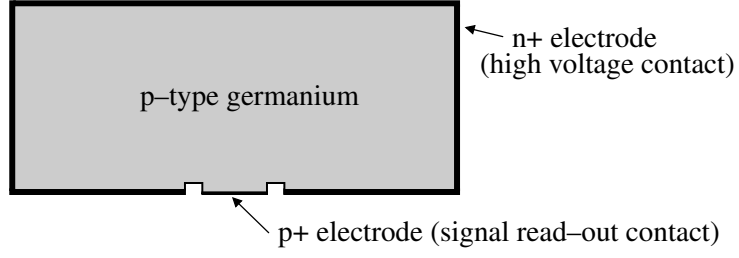


Figure 2. Sketch of a BEGe detector. The signal read-out electrode and the groove are not to scale. The plot shows a vertical section of the detector passing through the symmetry axis.

3.1 The electric field inside BEGe detectors

The pulse shape discrimination properties of BEGe detectors have been attributed to the peculiar internal electric field which is created by the small size of the read-out electrode. In Section 2.1 the space charge distribution inside the active volume (equivalent to the net distribution of acceptor impurities) was identified along with the electrode potentials as a source of electric field inside the detector. To better understand the two contributions, the linear superposition principle can be used to separate the potential into the two individual components:

$$\phi(\vec{r}) = \phi_0(\vec{r}) + \phi_\rho(\vec{r}) \quad (3.1)$$

where ϕ_0 is the potential calculated considering only the electrode potentials and no impurity charge ($\rho(\vec{r}) = 0 \forall \vec{r}$) and ϕ_ρ is the potential generated by the impurity charge distribution when grounding all the electrodes. Therefore, we can solve the following two problems and then add up the solutions:

$$\left\{ \begin{array}{l} \nabla^2 \phi_0(\vec{r}) = 0 \\ \phi_0|_{S_{cathode}} = V_{cathode} \\ \phi_0|_{S_{anode}} = V_{anode} \end{array} \right. \quad \left\{ \begin{array}{l} \nabla^2 \phi_\rho(\vec{r}) = -\rho(\vec{r})/(\epsilon_0 \epsilon_r) \\ \phi_\rho|_{S_{cathode}} = 0 \\ \phi_\rho|_{S_{anode}} = 0 \end{array} \right. \quad (3.2)$$

Similarly, since the electric field is determined by the linear relation $\vec{E} = -\nabla\phi$, it can be also separated into two components:

$$\vec{E}(\vec{r}) = \vec{E}_0(\vec{r}) + \vec{E}_\rho(\vec{r}) \quad (3.3)$$

where $\vec{E}_0(\vec{r}) = -\nabla\phi_0(\vec{r})$ and $\vec{E}_\rho(\vec{r}) = -\nabla\phi_\rho(\vec{r})$.

Figure 3 shows the electric potential and the electric field strength of the two contributions and their sum for the BE3830/s detector operated in its nominal configuration, i.e. cathode grounded, anode set at 3500 V and $\rho \sim 10^{10}$ impurity atoms/cm³.

Figure 3.a and 3.b show the electric potential and field strength generated only by the electrodes ($\phi_0(\vec{r})$ and $||\vec{E}_0(\vec{r})||$). The potential and the field show a sharp variation in the region close to the small-size p+ electrode. The field in the rest of the volume is so weak that the collection time would be longer than the characteristic recombination time and most of the charge would be lost.

Figure 3.c and 3.d show the electric potential and field strength provided only by the impurity charge distribution ($\phi_\rho(\vec{r})$ and $||\vec{E}_\rho(\vec{r})||$). For the considered BEGe detector the charge concentration is approximated by a uniform distribution. The resulting negative electric potential reaches its

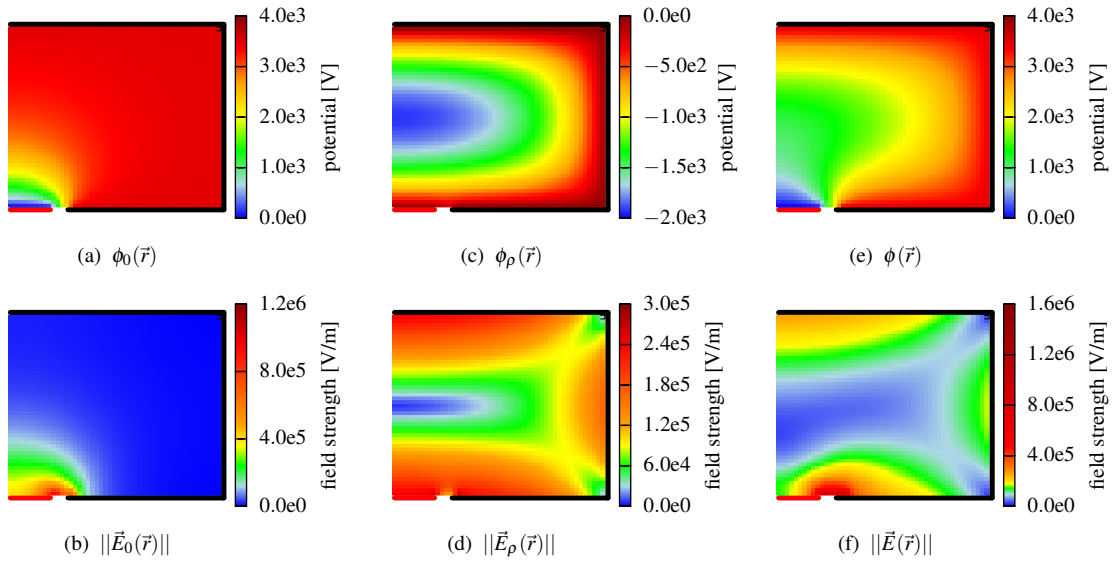


Figure 3. Simulated electric potential and electric field strength for different configurations of a BEGe detector. In (a) and (b) the electrode potential is considered, in (c) and (d) the charge distribution, and in (e) and (f) the sum of the two contributions. The plots show half of a vertical section of the detector passing through the symmetry axis. The cathode is drawn in red and the anode in black.

peak value in the middle of the detector. The direction of the electric field in the region close to the small cathode is opposite to that of \vec{E}_0 , whereas in the rest of the detector the field helps to move the charges produced close to the outer n+ electrode towards the central slice of the detector.

Figure 3.e and 3.f show the total electric potential and field strength ($\phi(\vec{r})$ and $\|\vec{E}(\vec{r})\|$). The potential close to the small p+ electrode is dominated by the electrodes contribution smoothed out by the opposite contribution of the impurity charge distribution field. In the rest of the volume the dominant contribution is provided by E_ρ . The effect of the E_ρ field is to bring the holes in the center of the detector while the field E_0 subsequently collects them to the read-out electrode. This peculiar way of charge transportation in BEGe detectors leads to the favorable signal shape as it will be discussed in the next sections.

3.2 Signal development in dependence of the interaction position

As given by equation (2.2), the weighting potential determines the charge induced by a cluster of charge carriers inside the detector on the read-out electrode. Figure 4 shows the weighting potential $\phi_w(\vec{r})$ and the strength of the weighting field $\|\vec{E}_w(\vec{r})\| = \|\nabla\phi_w(\vec{r})\|$ of the cathode in a BEGe detector. The weighting potential (similarly to ϕ_0 in Figure 3.a) has a sharp variation in the region close to the small-size p+ electrode and it is very weak in the rest of the detector volume (blue area in Figure 4). If an interaction occurs in the volume of weak ϕ_w , according to equation (2.2), the signal induced by the holes drifting towards the small cathode remains small until the charges arrive at about 1 cm away from the electrode and then rapidly grows until the holes are collected.

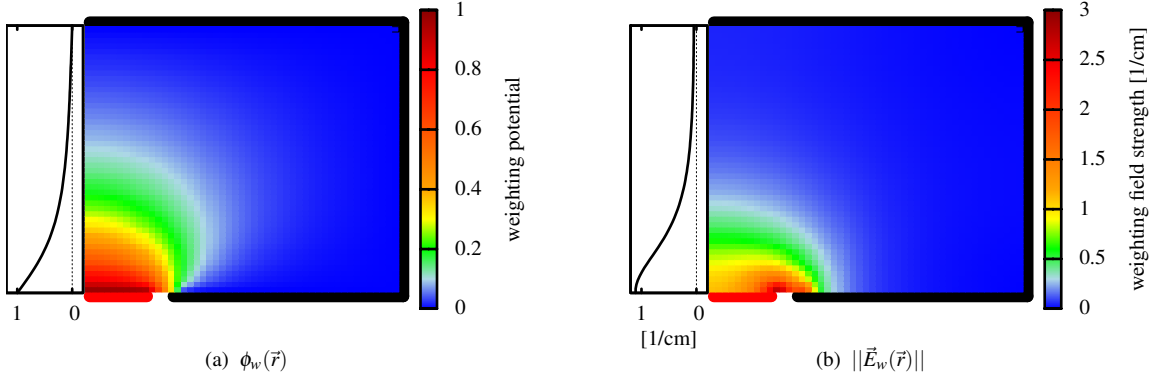


Figure 4. Weighting potential (a) and weighting field strength (b) of the small read-out electrode (cathode) computed for half of a vertical section of the BEGe detector passing through the detector symmetry axis (density maps) and for the symmetry axis (black lines in the side plots). The cathode is drawn in red and the anode in black.

On the other hand, in most of the active volume the electron contribution will be present only at the beginning of the pulse, since electrons are collected to the outer n+ electrode and the portion of the detector volume that is close to the outer surface is much larger than the portion close to the p+ electrode. This effect is further enhanced due to the fact that electrons move with velocities roughly two times higher than the holes. Moreover, the signal induced by the electron drifting will be relatively small, as most electron clusters move in the region of weak ϕ_w . Thus, the contribution of the electrons to the formation of the signals is expected to be negligible for most of the interaction positions.

Figure 5.a shows the electron and hole trajectories for three interactions in the “bulk” detector volume far from the p+ electrode. The holes follow the electric field (Figure 3.f) and are first transported into the middle slice of the detector, then drift towards the center of the detector and finally their trajectory bends towards the read-out electrode. It can be noticed that for all these events, the last part of the hole collection happens along a common path which is independent of the starting position. Accordingly, the last part of the induced signal is identical for the different events. Since the first part of the signal, induced by the holes and electrons in weak ϕ_w regions, is comparatively small, the signal shapes are essentially independent of the interaction position. This can be clearly seen in Figure 5.b, which shows the charge and current pulses corresponding to the trajectories from Figure 5.a. The only visible difference is the time shift of the rising part, which depends on the length of the charge carrier path to reach the strong ϕ_w region. It is important to stress that this type of almost indistinguishable signals originates from interactions in most of the detector volume, including corner regions. For further discussion we will refer to such signals as “type I” trajectories.

The shape of the current signals in Figure 5.b can be understood by differentiating the function in equation (2.2). The current induced at the cathode by a charge carrier is then given by:

$$I(\vec{r}(t)) = \frac{dQ(\vec{r}(t))}{dt} = q_{tot} \vec{v}(\vec{r}(t)) \cdot \vec{E}_w(\vec{r}(t)) \quad (3.4)$$

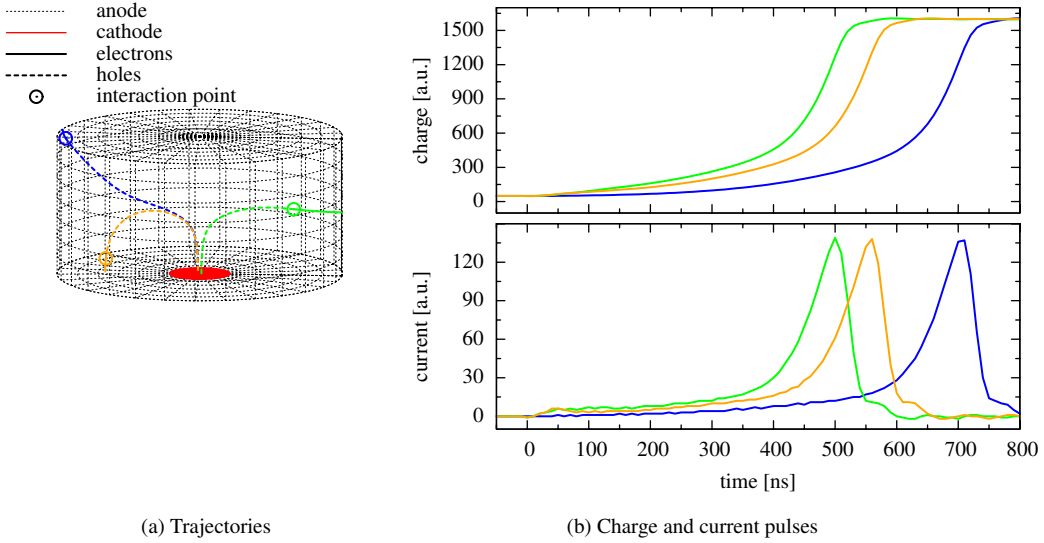


Figure 5. Simulated electron–hole trajectories (a) and corresponding charge and current pulses (b) for three events occurring in different places in the bulk detector volume far from the p+ electrode (“type I” trajectories). The small oscillation in the current signals after the peak originates from the experimentally measured FE and DAQ response the pulses are convolved with.

From this equation we can see that the induced current $I(\vec{r}(t))$ depends on the velocity $\vec{v}(\vec{r}(t))$ and the weighting field $\vec{E}_w(\vec{r}(t))$ at the position $\vec{r}(t)$ of the charge cluster. The charge carrier velocity can vary roughly between 5 cm/s and 10 cm/s [21], while E_w can increase by more than a factor of 20 close to the read–out electrode (see Figure 4.b). It is evident that E_w has a dominant effect on the current signal – the signals of “type I” trajectories in Figure 5.b feature a significant current peak at the end of the hole collection.

Two other types of less common trajectories can be identified when the interactions occur in the close vicinity of the groove and the small p+ electrode. Examples of these kind of events are displayed in Figure 6. The “type II” trajectories originate close to the p+ electrode (green and black color). In these events the holes are directly and quickly collected at the cathode. Now also the electrons drifting in the opposite direction provide a significant contribution to the signal, since they are now moving in a region of strong ϕ_w . The closer the interaction occurs to the cathode, the more important the signal induced by electrons becomes. The signal is fully dominated by the electron contribution for interactions within ~ 2 mm from the p+ electrode (black example in Figure 6). The induced charge signal rises quickly at the beginning and then, as they drift away from the cathode into the weaker ϕ_w regions, the signal growth slows down. The current peak appears at the very beginning of the collection time. For events occurring few mm to ~ 1 cm from the p+ electrode (green example in Figure 6) neither electrons nor holes traverse the full thickness of the strong ϕ_w region. So the main part of the signal is induced in a relatively short time and the rise time is thus faster. The current peak is amplified because contributions from both charge carrier types add up. The current amplification can be further enhanced if the interaction happens close to the inner edge of the groove, because here E_w is strongest (Figure 4.b).

Starting points in a zone close to the anode, ~ 1.5 cm from the detector symmetry axis, result in

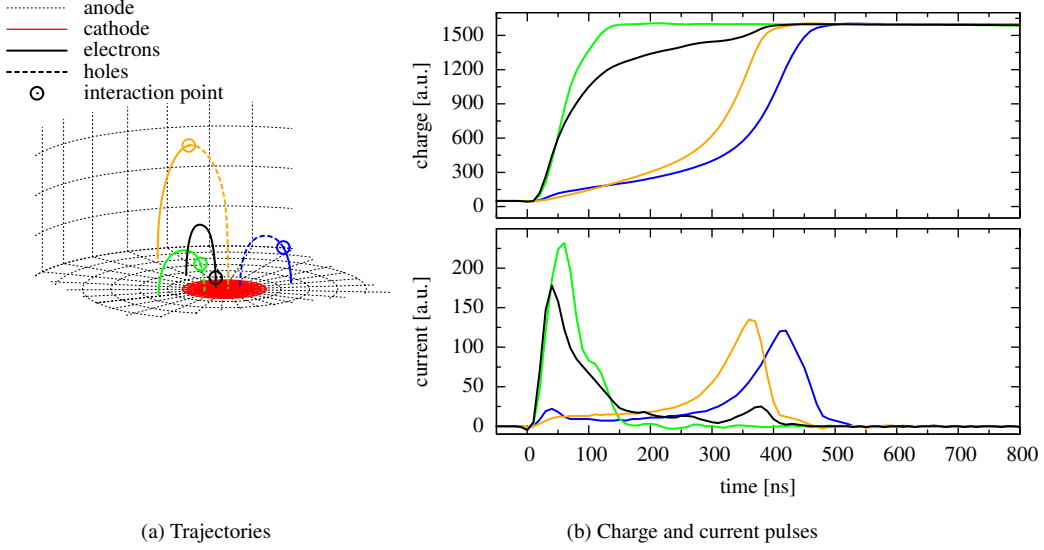


Figure 6. Simulated electron–hole trajectories (a) and corresponding charge and current pulses (b) for three events occurring next to the cathode and a “type I” event (orange line). For the green and black events (“type II” trajectories) both the electron and hole contribution are present at the very beginning of the signal. In the blue event (“type III”) the electron collection is quick and provides a characteristic kink in the first part of the signal.

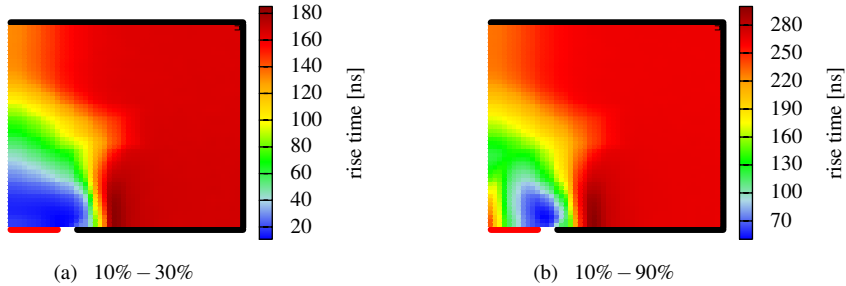


Figure 7. Signal rise times 10–30% (a) and 10–90% (b) as a function of the interaction position for a BEGe detector.

“type III” trajectories (shown blue in Figure 6). For these events the electrons are collected quickly, and since ϕ_w is still noticeable in this region, they provide a characteristic kink in the first part of the signal. This quick increase at the beginning causes the 10% to 90% rise time measurement to give higher values for these events than for the “standard” type I trajectory events.

The three types of signals and the extent of the volumes from which they originate can be better understood from the plots shown in Figure 7. The figure shows the rise times in the 10% to 30% and 10% to 90% intervals of the signal height, as a function of the interaction position. The type II trajectories originate in the volume close to the p+ electrode ($\sim 6\%$ of the active volume), distinguished by short rise times plus a small zone of longer rise times few mm away from the center of the electrode. The type III trajectory starting points can be identified in the area of increased rise

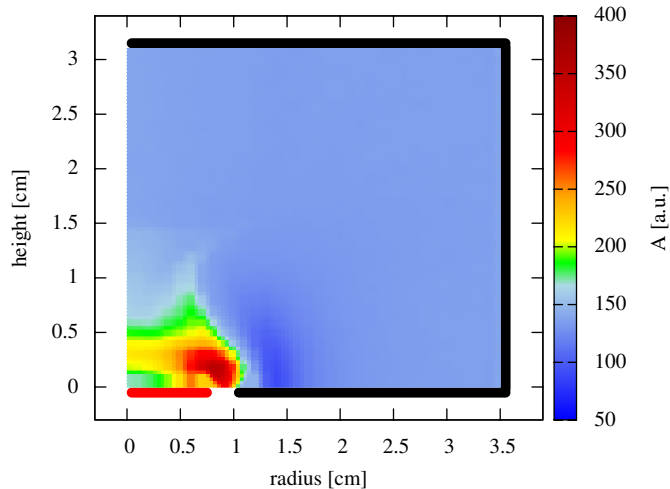


Figure 8. Distribution of the maximum current pulse amplitude A for simulated single interactions with unit energy as a function of the interaction point. A is constant in most of the detector volume (type I trajectories), but it is amplified in the region close to the cathode (type II trajectories). The region of lower A values close to the outer radius of the groove is an artifact due to the use of the pulse shape library with 1 mm step size. Here the charge collection time varies on scales smaller than the library grid with the effect that the averaging of library pulses leads to a reduction in current-peak amplitude. The effect is not present when the signals are generated directly without the use of the library.

time beyond the outer diameter of the groove ($\sim 1\%$ of the total active volume). Interactions in the rest of the detector volume result in the most common type I trajectories.

3.3 Discrimination between single-site and multiple-site events

In the previous subsection we have shown that most of the single interactions in BEGe detectors produce uniform signals (type I trajectories), differing one from the other only by the total charge collection times. In addition, the current signals have a simple shape with only a single narrow peak at the end of charge collection. These features can be exploited for a powerful discrimination of Single-Site Events (SSE) and Multiple-Site Events (MSE). A discrimination method based on the current signal amplitude was introduced in Ref. [7] and explained by using an empirical estimate of the weighting fields in BEGe detectors [8]. Here we recall the basic idea of the method and refine the discussion based on more accurate electric potential and field calculations.

For typical BEGe events the part of the hole trajectory that passes through strong E_w is always the same. Therefore, according to equation (3.4) the amplitude of the induced current signal depends only on the total charge of the considered hole cluster. Figure 8 shows the value of the maximum current pulse amplitude A for simulated single interactions with unit energy deposition, as a function of the interaction position in a vertical section of a BEGe detector. We see that the parameter A is constant in most of the detector volume (corresponding to the typical type I trajectories) except for the region close to the p+ electrode, where the type II trajectories with amplified

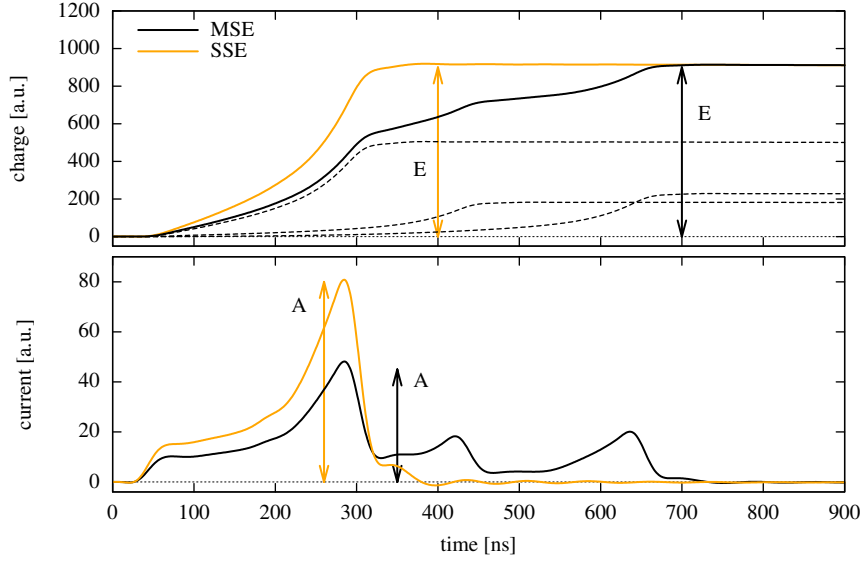


Figure 9. The upper panel shows typical charge pulses for SSE and MSE while the lower panel shows the corresponding current pulses obtained as the derivatives of the charge signals. The dashed lines in the top panel show the contributions of the individual single interactions to the total charge pulse in the MSE.

current signals originate (Figure 6).

The Pulse Shape Discrimination (PSD) method uses the parameter A normalized to the total event energy E : the A/E ratio. The concept is depicted in Figure 9. For SSE, all energy is transferred to a single charge cluster – it follows that A/E is constant for such events. In MSE, the total event energy is shared between several spatially-separated charge clusters (Figure 9 illustrates the case of three clusters). Since the current peaks are narrow and the charge collection time is position-dependent, the A/E ratio will be smaller than the constant value given by SSE.

The region of amplified current signals (approximately a hemisphere of a ~ 13 mm radius from the center of the p+ electrode in Figure 8, corresponding to $\sim 5\%$ of the detector active volume) was already identified in Refs. [7, 8]. It limits the efficiency of our PSD method, since interactions from MSE occurring in this volume can have their A/E ratio amplified above the SSE discrimination threshold. On the positive side, this effect can be used to identify surface events occurring on the p+ electrode and groove surfaces.

4. Validation of the simulation

The implementation of BEGe detectors in the MAGE Monte Carlo simulation framework, accurately reproducing their radiation detection efficiency, was presented already in [7, 8, 21, 22]. Here we report only the measurements carried out to validate the pulse shape simulation. Two sets of measurements were performed for this purpose. First we used a collimated ^{241}Am source to generate well localized interactions and to compare directly the pulse shapes for different interaction positions close to the surface of the detector. Then, a ^{228}Th source was used to investigate the distribution of the pulse rise times and of the parameter A/E as a function of the energy for events in the whole detector volume.

4.1 The experimental setup

The detector used for the validation measurements was the BE3830/s BEGe detector described in Section 3. The front end read out of the signals was performed with the Canberra charge sensitive preamplifier 2002CSL [20], which is integrated in the housing of the detector. The preamplifier output was digitally recorded with a 4 channel N1728B CAEN NIM flash analogue–digital converter [23] running at 100 MHz sampling frequency with a precision of 14 bits. This module is fitted with a USB connection for communication with a PC. To control the digitizer setup, the acquisition parameters and the storage of the data, the PC was interfaced to the NIM module by using the TUC software [24]. We recorded pulse shapes with a total length of 40 μs including a baseline before the signal of $\sim 10 \mu\text{s}$. The energy reconstruction was performed off–line by using the GELATIO software [25] implementing the *Moving Window Deconvolution* approach [26] and several digital filters were applied to the data to reject pile–up and noise events.

To perform the ^{241}Am measurements, a mechanical device was built to allow the movement of collimated sources with sufficient accuracy along the diameter of the front face and circularly around the symmetry axis of the detector. The collimator had a hole of 1 mm diameter and a length of 34 mm. These ^{241}Am collimated measurements were accurately simulated by using a conical beam of 59.5 keV photons.

4.2 Pulse shape comparison with low energy gamma–ray beams

Using a collimated beam of low energy gamma–rays (59.5 keV) from a ^{241}Am source allows to obtain pulse shape data with well defined interaction coordinates. As the 59.5 keV photons penetrate only a few millimeters underneath the germanium crystal surface and the volume spread of their energy deposition is of similar size, the narrow beam can be used to study pulse shape position dependence with few millimeters resolution. As the topologies of the individual photon interactions are statistically variable, an average signal was calculated for each position of the collimated source. This procedure of averaging over many signals for a given position also helped to significantly reduce the influence of the electronic noise.

The pulse shape comparison included scanning along the diameter of the detector and a circular scan at a fixed distance from the symmetry axis of the detector. The radial scan allows the study of pulse shapes as a function of the distance from the center. With the circular scan the rise time variations due to the drift velocity anisotropy caused by the crystal lattice structure were investigated.

The radial scan was performed by moving the collimated ^{241}Am source along the radius of the detector on the top surface of the end–cap in steps of 0.5 cm. The simulated hole trajectories for each collimator position and the average signals are shown in Figure 10. Good agreement is observed between the simulated and experimental pulses.

As an increase of the radius value corresponds to an increment of the hole collection time, the total rise time should increase as the interaction point moves away from the symmetry axis. However, according to the discussion in Section 3.2, for interactions far from the p+ electrode the pulse shapes are expected to be different only at the very beginning. Looking at Figure 7.b BEGe signals along the top surface show only minimal variation of the 10% – 90% rise time. In order to

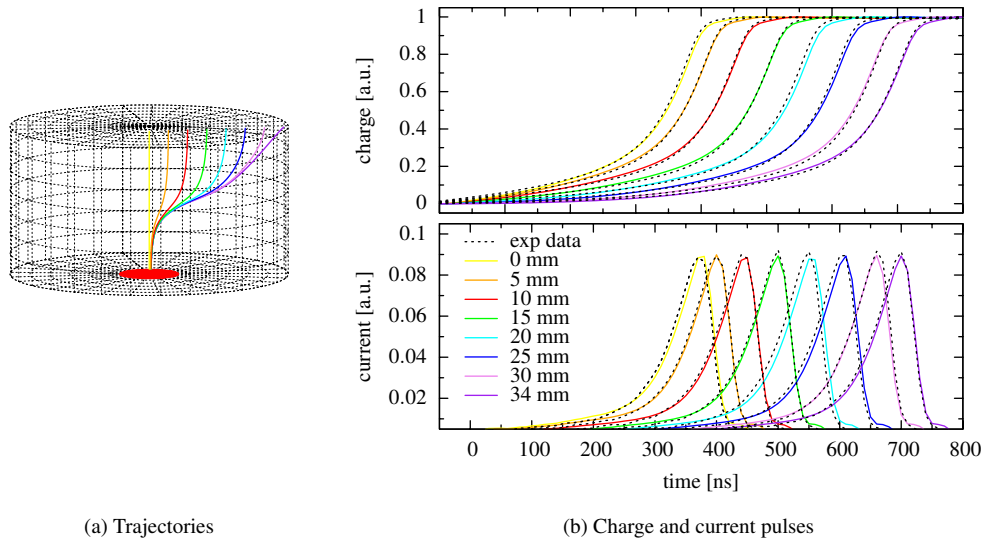


Figure 10. Simulated hole trajectories (a) and average signals (b) computed for several interaction points at different radii on the detector top surface. The interactions were obtained by moving a 1 mm collimated ^{241}Am source on the top surface of the end-cap along the radial direction. The small deviation present at the very beginning of the signals can be related to the fixed grid width used for defining the library of pulses.

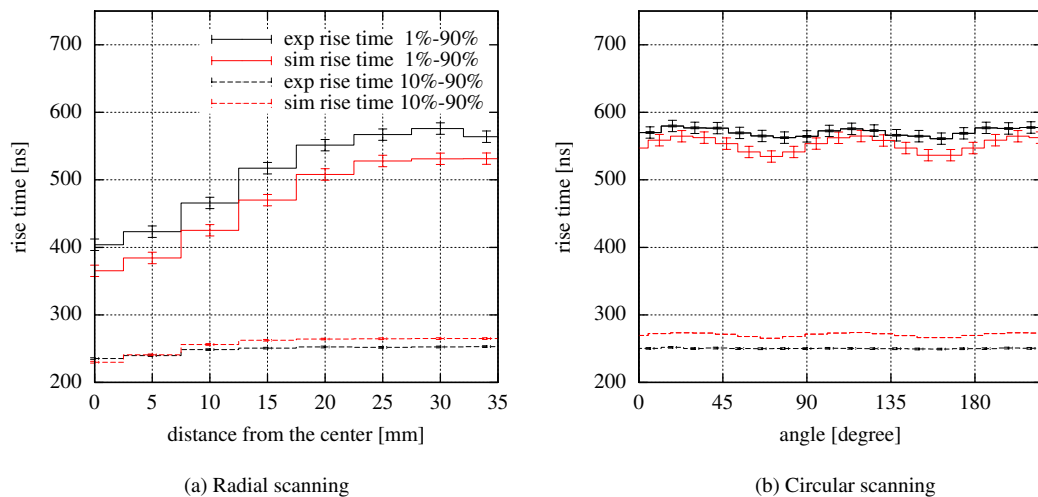


Figure 11. 1% – 90% and 10% – 90% rise time values reconstructed from the simulated and experimental average pulses for different interaction points. The interactions were obtained by moving a 1 mm collimated ^{241}Am source on the top surface of the end-cap, along the radial direction (a) and around a part of a circle centered on the detector symmetry axis (b). The rise time uncertainty was estimated by determining the spread of rise time values computed from several measurements at one source position.

observe a significant effect, the rise time between 1% and 90% has to be considered. This can be clearly seen in Figure 11.a for both the experimental and simulated data.

For the circular scan the collimated ^{241}Am source was moved around a circle with a radius of 34 mm centered on the detector’s symmetry axis on the top surface of the end-cap with a $\sim 10^\circ$

step. The drift velocity anisotropy arises due to the charge carriers drifting at different angles relative to the detector’s crystallographic axes. Like with the radial scanning, also in this case the differences occur only in the first part of the charge collection, and the 1% – 90% rise time has to be used. The comparison of circular–scan rise times as a function of the circumference angle from the simulation and the experiment is shown in Figure 11.b.

Although the experimental data show a behavior coherent with the simulation in both the radial and circular scans, the agreement is only qualitative. The 1% – 90% rise times of the simulated data are systematically shifted by 20 – 40 ns (5% – 10% of the total rise time) to lower values than the experimental data. In contrast, the 10% – 90% rise times of the simulated data are shifted by \sim 20 ns to higher values than the experimental data. The change in the sign of the discrepancy is due to differences in the shape of the average pulses. Furthermore, the oscillation amplitude due to crystal anisotropy in Figure 11.b is higher in the simulation than in the experimental data by 30%. Unlike the experimental data, the simulation shows a residual oscillation of about 5 ns also in the 10% – 90% rise time plot. From these comparisons we can conclude that the simulation is more sensitive to the drift velocity anisotropy than the real detector and probably further small discrepancies in the signal calculation are present. This allows us to identify several areas of possible improvements of our simulation, including the accuracy in the geometry definition (especially important in case of the p+ electrode), the finite grid width used for defining the library of pulses and the charge carrier mobility model parameterizations (defined by using a different crystal [18]). Also further measurements could be performed to characterize the position dependence of the BEGe signals (e.g. by performing collimated ^{241}Am scans also along side and back surfaces, and by doing collimated single–Compton scattering measurements with higher–energy sources to sample also the internal detector volume).

4.3 Rise time and A/E distributions studies

A different approach for validating the simulation is given by the comparison of the rise time and the A/E distributions as a function of the event energy. Unlike the ^{241}Am measurements which create interactions restricted to a region close to the detector surface, 2.6 MeV gamma–rays from a ^{228}Th source interact in the whole detector volume and can deposit energy at several sites before escaping or being absorbed. Under these circumstances, the distributions of the rise times and of the parameter A/E are sensitive to the electric and weighing potential in the whole detector and thus are useful for testing the accuracy of the simulation.

For this study a long measurement was performed with a ^{228}Th source³. The detector was located in the LNGS underground laboratory and surrounded by a lead shielding in order to reduce the background due to cosmic rays and natural radioactivity.

Figure 12 shows the distribution of the 10% – 90% rise time as a function of the energy in the range including the Double Escape Peak (DEP) at 1592.5 keV and the Full Energy absorption Peak (FEP) at 2614.5 keV of ^{208}Tl . Both the experimental and simulated data show a similar structure of the distribution, with a high density band at rise time values around \sim 270 ns. The region below

³In the simulation only the ^{208}Tl isotope was considered resulting in some missing gamma–ray interactions at energies below \sim 1.8 MeV as compared to the experimentally measured spectrum. Moreover, the simulation does not include the SEP Doppler broadening of the positron annihilation energy which is determined by the electron momentum distribution in germanium.

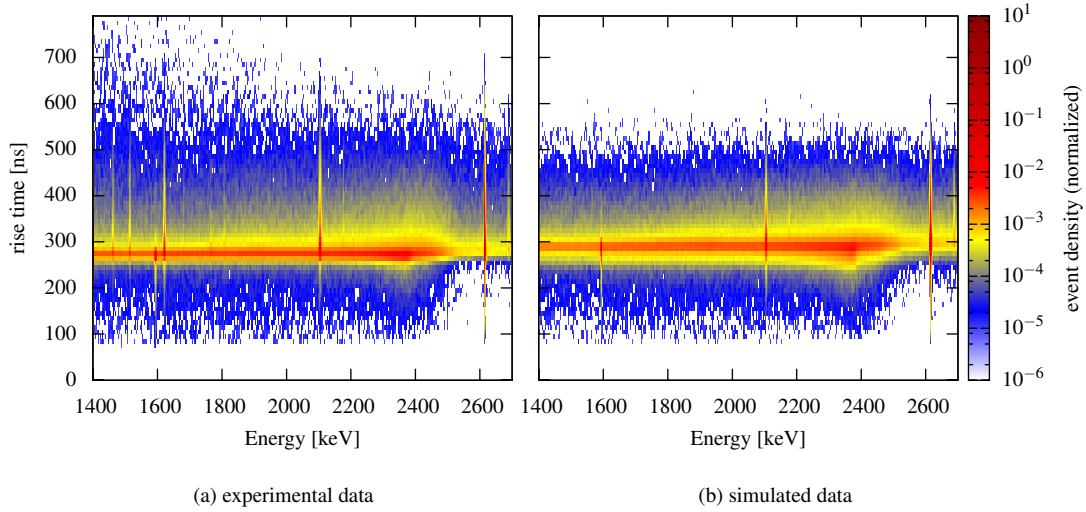


Figure 12. Experimental and simulated distributions of the 10% – 90% rise time values as a function of energy from the ^{228}Th measurements. In the simulation only ^{208}Tl is considered. The density plots are normalized according to the number of events in the 2.6 MeV FEP.

the band contains the fast pulses resulting from events with type II charge collection trajectories described in Section 3.2 generated by interactions close to the p+ electrode. The region above the band is composed mainly of MSE events which have typically slower rise times than SSE (this is visible in Figure 9). Consistently, all the full absorption peaks (consisting typically of multiple Compton scatterings followed by photo-absorption) show an important tail in this region, while the DEP (containing the typically single-site e^- and e^+ absorptions after pair-production) has a very weak tail. According to the simulation, events occurring in a small volume close to the outer radius of the groove (type III charge collection trajectories in Section 3.2) are also expected to have increased rise times. It is however evident from the plot that the simulation creates events with rise times only up to 600 ns while the experimental data show a significant number of events with rise times > 600 ns ($\sim 1.5\%$ of the total).

The simulated and experimental data can be compared in more detail in Figure 13 which shows distributions of the 10% – 90% rise time in narrow energy regions around the DEP, the Compton continuum at 2 MeV and the 2.6 MeV FEP. For the DEP and FEP distributions the contribution from their Compton continuum backgrounds is subtracted. While the shape of the distribution below ~ 250 ns (corresponding to the fast signals from the type II events) is reproduced fairly well, the main peak and the region above it show some differences between the simulation and experimental histograms. As we already noted in the previous subsection, our simulation is not perfect in some aspects. The charge carrier mobility model is likely responsible for the shift of the rise time histogram maximum, while the enhanced drift velocity anisotropy in the simulation could explain the greater width of the peak. Minor discrepancies in the geometry description of the p+ electrode and the groove, as well as the finite grid width of our pulse library could account for the small ~ 20 ns shift between the start of the experimental and simulated histogram, as well as for a

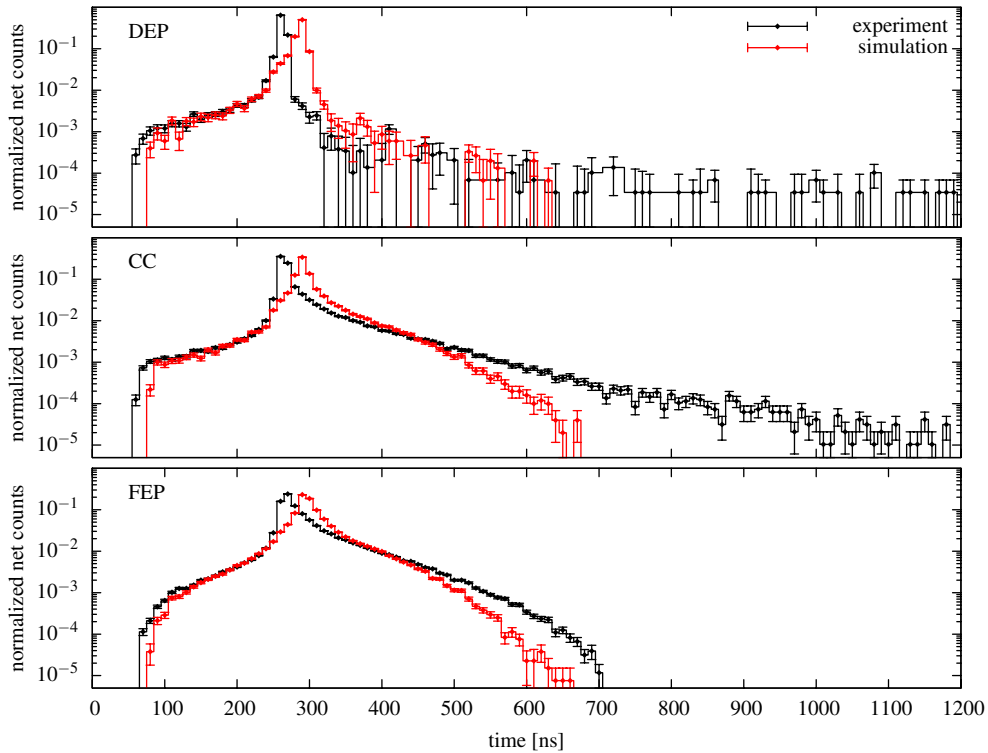


Figure 13. Experimental and simulated distributions of the rise time for the region around the DEP, the Compton continuum at 2 MeV (CC) and the 2.6 MeV FEP. The error bars take into account only the statistical error. The DEP and the FEP distribution are corrected for the background. The integrals of the histograms are normalized to one.

part of the excess long rise time events in the experiment. In addition, some pile-up events show up with very long rise times up to a few μs .

However, most of the signals with rise time above ~ 500 ns (most clearly visible in the Compton continuum histogram in Figure 13) are expected to come from the region close to the $n+$ surface. The Li-infused n -side of the p - n junction can not be fully depleted of conduction band electrons and forms the well known dead layer covering the outer surfaces of p -type Ge detectors. The appearance of pulses with long rise times in $n+$ surface interactions was noticed before with conversion electron measurements in Ref. [27] and can be clearly observed by irradiating the detector with ^{241}Am gamma rays, as reported in Ref. [28]. It can be assumed that the electric field near the $n+$ surface has insufficient strength to effectively move the charge carriers. In turn, the drift time is extended and part of the charge can be lost by trapping. This effect can explain the observed slow pulses in our experimental data. It is also consistent with the fact that the DEP and FEP peak regions in Figure 13 show a much smaller excess of slow pulses than the Compton continuum region. This is due to the charge carrier losses moving the event in the energy spectrum away from the peak regions into the lower energy continuum. As the peak histograms have the continuum background subtracted, the slow pulse contribution is removed as well. The content of these slow pulses in the Compton continuum region was estimated to be $\lesssim 4\%$. The study of these $n+$ layer effects can be

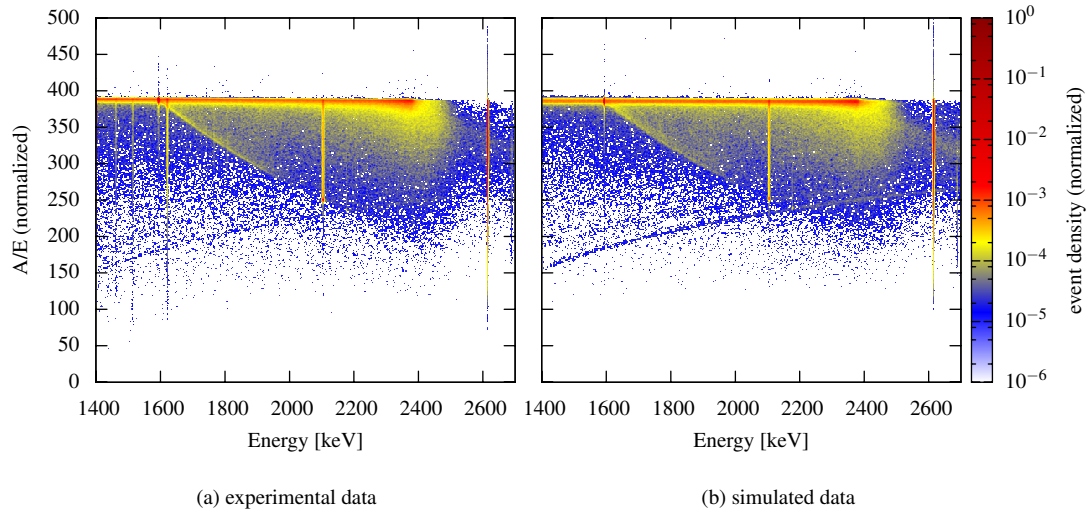


Figure 14. Experimental and simulated distributions of the A/E parameter as a function of energy for ^{228}Th source measurement. In the simulation only the ^{208}Tl is considered. The density plots are normalized according to the number of events in the 2.6 MeV FEP.

in future augmented by our pulse shape simulation if the spatial resolution of the field calculation is improved to better cover the 0.7 mm thick region.

Figure 14 shows the distribution of the parameter A/E as a function of energy. The plots show a well defined horizontal band of increased event density, composed of SSE. Below the band the region of MSE extends. Above the band one can see a region of events with amplified current signal occurring close to the p+ electrode as already discussed in Section 3.3. This interpretation of the A/E distribution was previously validated by coincident Compton scattering measurements (providing clean SSE samples at several energies) and by collimated ^{228}Th measurements (providing DEP events restricted to the detector volume close and far from the p+ electrode) [7, 8]. Another visible feature in the plot is a diagonal band between the DEP and the Single Escape Peak (SEP), composed of pair-production events (as explained in Ref. [7, 8]), and two weak narrow bands in the MSE region, which are caused by cascade summing events⁴. There is no significant difference between the plots from the experimental and simulated data apart from the ^{212}Bi lines present in the measurement and not in the simulation. All the features of the A/E distribution are reproduced by the simulation.

Figure 15 shows the A/E distribution for energy slices around the DEP, the Compton continuum at 2 MeV and the SEP at 2103.5 keV. As in Figure 13 the histograms from the DEP and SEP are corrected for the Compton continuum background contribution. The simulation is in good agreement with the experimental data in all three energy regions. However, in the Compton continuum region one can see a small deviation at low A/E values. This excess can be associated

⁴The two visible additional bands result from the summation of the SSE in the Compton continuum with either the 511 keV or 583 keV full energy gamma absorption from the ^{208}Tl cascade. This results in the energy of the event being shifted but the A value staying the same since the SSE from the Compton scattering still dominates the current signal.

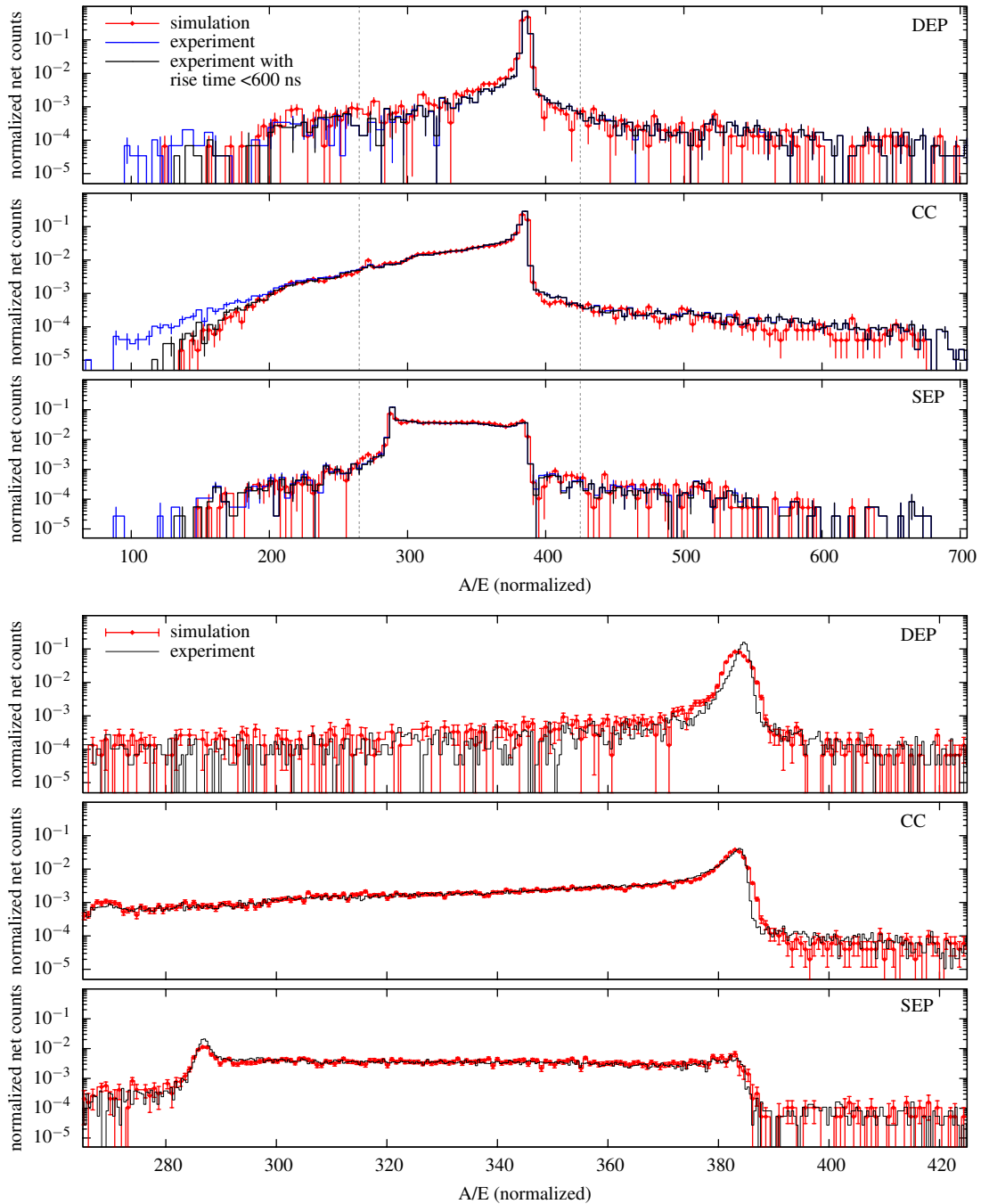


Figure 15. Experimental and simulated distribution of the A/E parameter in the region around the DEP, the Compton continuum at 2 MeV (CC) and the 2.6 MeV FEP. The error bars take into account only the statistical error. The DEP and the SEP distribution are corrected for the background. The integrals of the histograms are normalized to one. The top plots show the experimental distribution before and after a cut on the rise time to remove slow pulses not included in the simulation. The regions defined by the gray vertical lines are enlarged in the bottom plots.

to the presence of the near n+ electrode slow pulses in experimental data. It can be assumed that by stretching the charge carrier cluster, the peak in the current signal gets wider and its height is reduced. By applying a cut on the rise time at 600 ns (black histogram in Figure 15) the agreement in the tails improves significantly.

The plots at the bottom of Figure 15 show the A/E histograms of Compton continuum, the SEP and the DEP focused on the region near the SSE-band peak (near $A/E \sim 385$). It is apparent mainly from the DEP plot that the simulated SSE peak is a little wider than in the experimental data and the shape is slightly different. This discrepancy is likely the result of the same simulation inaccuracies as discussed earlier. The Compton and SEP histograms show that for MSE-dominated distributions the overall agreement is significantly better. This demonstrates that the partitioning of the energy depositions into individual charge clusters (performed by the Monte Carlo block) is simulated accurately.

5. Background rejection and signal identification studies

A direct application of the BEGe detector simulation was the study of the Pulse Shape Discrimination (PSD) efficiency in separating SSE from MSE introduced in the Section 3.3. First we compared the performances of the PSD applied to experimental and simulated sets of measurements with ^{228}Th and ^{60}Co sources placed outside the detector housing. We then used the simulation to study the survival probabilities of decays which occur inside the Ge crystal. The focus of this investigation concerned the $0\nu\beta\beta$ decay signal of ^{76}Ge and the background signals created by the decays of the radio-isotopes ^{68}Ge and ^{60}Co . The latter are produced by cosmic ray interactions during germanium detector production above ground. These radio-isotopes are one of the most critical backgrounds in ^{76}Ge neutrinoless double beta decay search. However it is challenging to study experimentally the decays of these isotopes inside the Ge crystal. The simulation tools introduced in this paper represent a powerful method to investigate quantitatively the PSD performance on these backgrounds.

5.1 Comparison of pulse shape discrimination of simulated and experimental data

The comparison was performed using two high-statistic data sets generated by a ^{228}Th source (^{208}Tl in the simulation) placed 2 cm away from the Al end-cap and a ^{60}Co source placed at the end-cap (on the detector symmetry axis). The recorded signals (10 ns time step) are smoothed by triple 50 ns moving window averaging. The current signal is then reconstructed by 10 ns differentiation of the smoothed charge pulse. Finally, interpolation into 1 ns time steps is performed before measuring the current pulse amplitude A . This procedure was found to provide the optimal resolution for A .

The SSE-rich Compton continuum of the 2.6 MeV ^{208}Tl gamma-line at 2.6 MeV is used to calibrate the slight energy dependence of the SSE band in the A/E distribution. This procedure was described in detail and validated in Refs. [7, 8]. The multi-site events, which have lower A/E values than single-site events, are removed by performing the PSD cut at a constant offset from the center of the SSE band (visible as a high-density band at $A/E \sim 385$ in Figure 14).

The efficiency of the cut is tuned by the definition of the offset. In Refs. [7, 8], the cut offset was defined according to the spread of the SSE band in the DEP region and the resulting DEP

Table 1. Percentage of survived events from a ^{228}Th and a ^{60}Co measurement after the PSD cut in different regions of interest (ROI) for the three cut definitions. The results for DEP, SEP, FEP, SP and the two ^{60}Co lines at 1173 keV and 1332 keV (FEP1 and FEP2 in the table) are calculated using the net peak areas. The CC region corresponds to an 80 keV wide section of Compton continuum centered at 2039 keV (^{76}Ge $Q_{\beta\beta}$). The uncertainties given in parenthesis for the least significant digits include statistical as well as systematic uncertainties estimated by cut parameter variation. The ^{208}Tl FEP and the ^{60}Co FEP1 lie outside of the range covered by the calibration of A/E energy dependence (1.35 MeV to 2.38 MeV) so can be subject to additional systematic errors.

source	ROI	experimental	simulated		
		DEP	DEP	SEP	SP
		fixed to 90%	fixed to 90%	fixed to 5.45%	fixed to 0.08%
^{208}Tl	DEP	0.900 (11)	0.900 (14)	0.84 (3)	0.61 (15)
^{208}Tl	SEP	0.055 (6)	0.079 (15)	0.055 (3)	0.038 (11)
^{208}Tl	FEP	0.073 (4)	0.12 (2)	0.088 (5)	0.059 (17)
^{208}Tl	CC	0.341 (14)	0.42 (3)	0.357 (17)	0.25 (7)
^{60}Co	FEP1	0.113 (6)	0.138 (17)	0.105 (6)	0.07 (2)
^{60}Co	FEP2	0.106 (6)	0.133 (17)	0.102 (6)	0.07 (2)
^{60}Co	SP	0.00080 (16)	0.0021 (7)	0.0012 (3)	0.0008 (3)
^{60}Co	CC	0.0082 (7)	0.012 (3)	0.0073 (9)	0.0043 (16)

acceptance was close to 90%. However, using this definition of the PSD cut on the simulated data is expected to create a biased result, since the profile of the SSE–band in our simulation has a different shape and spread than the one extracted from the experimental data (see Figure 15 and discussion in the previous section). On the other hand, the profile of the multi–site event region is dominated by the partitioning of the charge clusters, so the overestimation of anisotropy or other limitations in the simulation have a relatively smaller effect on MSE as compared to SSE distribution (see Figure 15).

To avoid the effect of the SSE–band discrepancy in the simulation results, we developed alternative definitions of the A/E cut offset. For experimental data we apply cut offset that retains a fixed acceptance of the net area of the DEP at 90%, maintaining compatibility with the previously published results. The survival fractions for ^{228}Th and ^{60}Co are listed in the “experimental” column of Table 1. The results are very similar to those obtained in previous works – the small differences as compared to [7] are mainly due to data treatment⁵ and the results in [22] differ due to a different implementation of the analysis. To be able to employ the simulation to estimate a realistic experimental survival probability both in SSE–dominated and MSE–dominated data, three different versions of the PSD cut were applied to the simulated data. The cut A/E offsets were defined by fixing survival fractions in a different peak region for each of the three cuts: 1) in the

⁵The different size of the detector used in [7] and geometry of its electrode was found to cause no visible difference in the results if the same data treatment is applied. Only the result for the Compton continuum region is significantly different, due to a larger distance of the source from the detector, resulting in fewer cascade summing MSE.

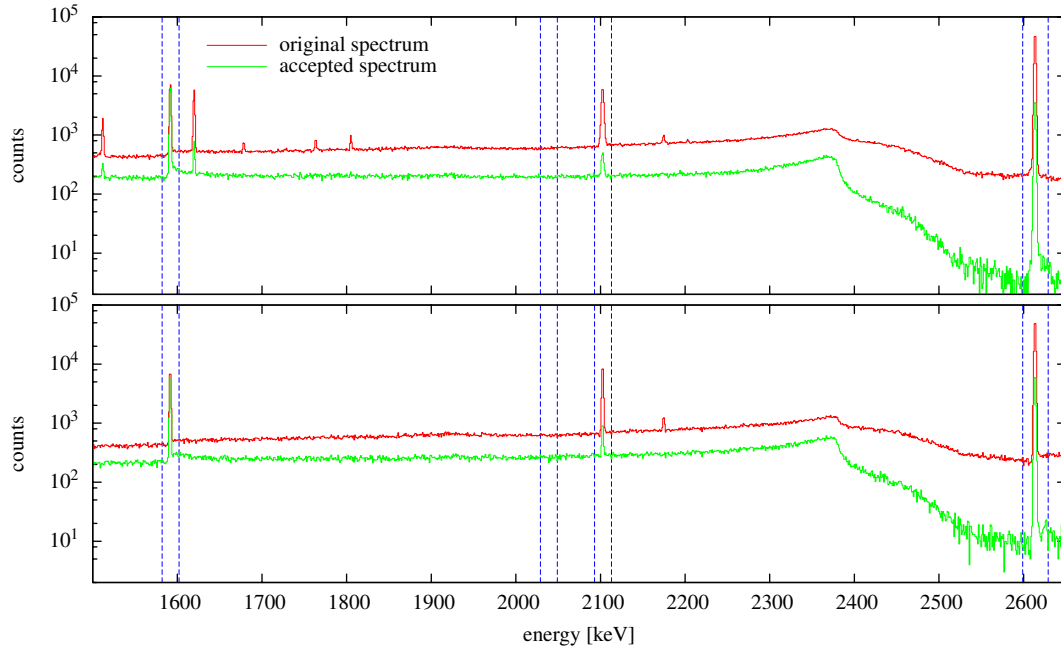


Figure 16. Experimental (top) and simulated (bottom) energy spectra for a Th source before (red line) and after (green line) applying the PSD cut.

DEP region; 2) in the MSE-dominated SEP of ^{208}Tl ; 3) in the highly-MSE dominated Summation Peak (SP) of the two ^{60}Co gamma-lines. The A/E offsets of these cuts is tuned to be equivalent exactly to the experimental data cut with 90% acceptance of DEP events, i.e. the SEP-based cut is adjusted to 5.45% SEP survival and SP-based cut to 0.08% SP survival (see the DEP, SEP and SP entries in the “experimental” column of Table 1). The results are shown in the last three columns of Table 1. It can be seen that the agreement with the experimental data for Compton continuum⁶ and the MSE dominated FEP and SP regions significantly improves when the SEP-based cut is used as compared to the DEP-based cut, while the DEP survival is accordingly underestimated. The SP cut results suffer from a higher uncertainty due to the very small number of events remaining in the SP after cut, nevertheless the agreement with experimental data is still reasonable in the highly MSE-dominated regions. We can conclude that the more similar is the event topology between the data region used for cut calibration and the studied region, the better is the agreement between simulated and experimental results. Figure 16 shows the simulated and experimental ^{208}Tl spectra before and after applying the PSD cut, using the 90% DEP cut definition.

5.2 Survival fractions of decays internal the Ge crystal

In the last part of our study we applied the PSD to simulated ^{60}Co , ^{68}Ga decays and $0\nu\beta\beta$ decays of ^{76}Ge , distributed inside the Ge-detector volume. The aim was to evaluate the $0\nu\beta\beta$ -signal acceptance by our PSD method and to determine the suppression power of the intrinsic cosmogenic backgrounds. Figure 17 shows the spectra of internal $0\nu\beta\beta$, ^{60}Co and ^{68}Ga before and after the

⁶Part of the discrepancy in the ^{208}Tl Compton continuum region arises due to the near n+ layer slow pulses, not included in the simulation.

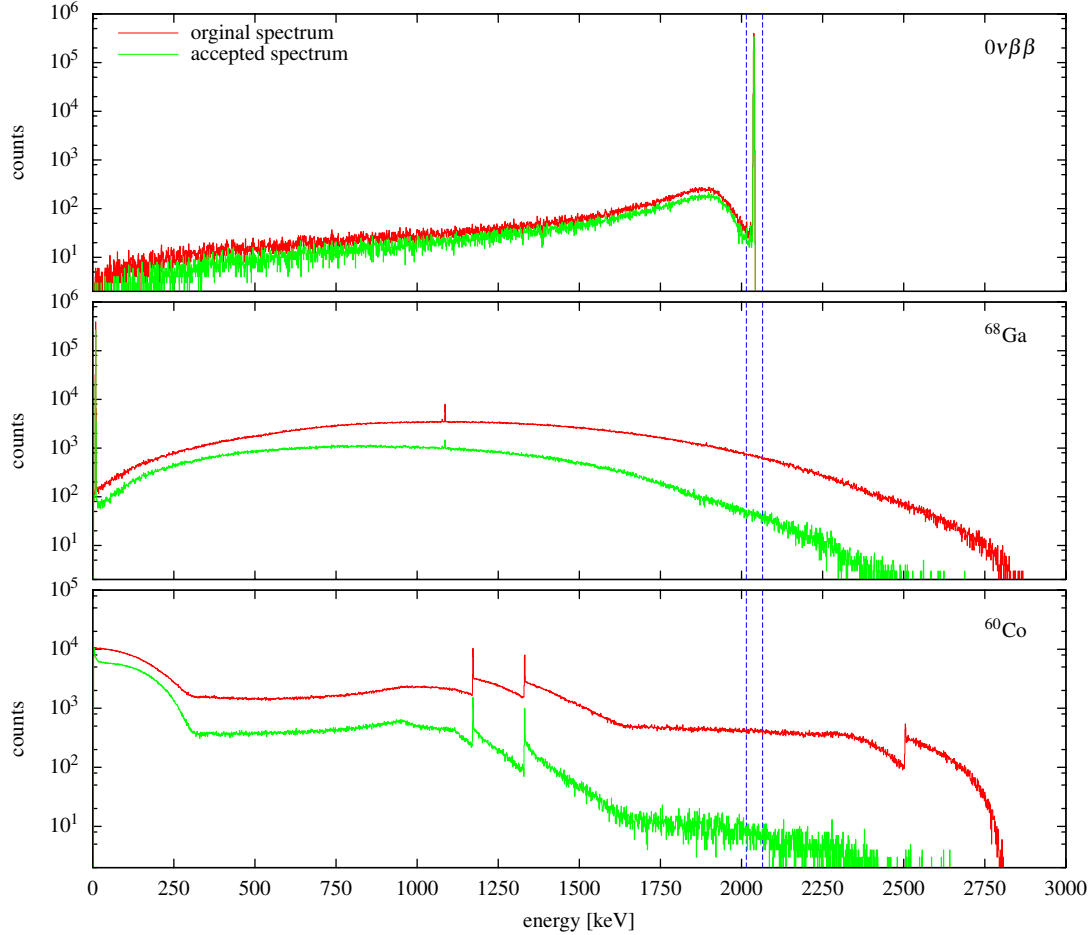


Figure 17. Simulated spectra of $0\nu\beta\beta$ decays (top), ^{68}Ga (middle) and ^{60}Co (bottom) inside a BEGe detector before (red line) and after (green line) the PSD cuts.

PSD cut using the DEP-based cut definition. The resulting survival fractions in the energy regions around the ^{76}Ge $Q_{\beta\beta}$ are summarized in Table 2, including the DEP-based, SEP-based and SP-based PSD cut definitions. According to the comparison reported in the previous section, we assume that the most realistic value for survival probability is provided by the cut calibrated in the data region with the most similar event topology, i.e. the DEP-based cut for the $0\nu\beta\beta$ peak, the SEP-based cut and SP-based cut respectively for the Compton continuum region at 2 MeV of ^{68}Ga and ^{60}Co (highlighted values). In cases when the MSE content of the region used for calibration is higher than in the studied events, the calculated survival probability will be underestimated, and vice versa.

The $0\nu\beta\beta$ spectrum shows a peak at the $Q_{\beta\beta}$ energy and a tail extending to low energies due to the events in which part of the total energy is either lost in the dead layer or escape the detector. Since the electrons generated by $0\nu\beta\beta$ decay events have a significant probability to emit a bremsstrahlung photon, not all the events in the $Q_{\beta\beta}$ peak and in the tail are SSE. The MSE contamination is similar to that in the DEP of ^{208}Tl . However, as the energy of the $0\nu\beta\beta$ decay event is higher than in DEP events, also the probability of bremsstrahlung and in turn of an MSE

Table 2. Percentage of survived events of $0\nu\beta\beta$ -decays and of internal sources of background after the cut in an 80 keV wide region centered on the ^{76}Ge $Q_{\beta\beta}$ of 2039 keV. The highlighted numbers represent the most realistic predictions for experimental survival probabilities assuming experimental PSD cut with DEP fixed to 90%. The uncertainties given in parenthesis for the least significant digits include statistical as well as systematic uncertainties estimated by cut parameter variation. The ^{60}Co result has an additional systematic uncertainty due to a small difference on the event topology between the SP region and the studied region.

source	DEP fixed to 90%	SEP fixed to 5.45%	SP fixed to 0.08%
$0\nu\beta\beta$	0.86 (3)	0.77 (3)	0.57 (13)
^{68}Ga	0.067 (11)	0.045 (3)	0.032 (7)
^{60}Co	0.019 (4)	0.0130 (11)	0.009 ($^{+4}_{-2}$)

interaction is higher and the PSD cut survival probability is thus slightly lower.

The decay chain of the cosmogenic ^{68}Ge consists of an EC decay into a ^{68}Ga , which eventually decays with 1.13 h half-life into ^{68}Zn via EC (11%) and β^+ decay (89%). The positron has an energy endpoint of 1.9 MeV, thus to produce events at the ^{76}Ge $Q_{\beta\beta}$ (2039 keV) its absorption has to be accompanied by an energy deposition from its annihilation photons. Such events have a topology resembling that of SEP events (strong electron/positron interaction combined with a weaker 511 keV gamma-ray interaction) and thus a comparable survival probability.

The ^{60}Co spectrum shows the two characteristic peaks at 1173.2 and 1332.5 keV generated in cascade. As the decay occurs inside the detector, the probability of a coincident detection is high, resulting in the summation peak at 2505.7 keV. Moreover, the electron associated to the β^- decay of ^{60}Co to ^{60}Ni (endpoint energy of 318 keV) is also absorbed leading to the peculiar ‘‘triangular’’ tail at the high-energy side of the peaks. The events in the $Q_{\beta\beta}$ region are a result of the cascade gamma and beta summation and consequently their topologies are highly multi-site, leading to suppression by a factor of 100.

6. Conclusions and outlook

In this paper we discussed the development of an integrated simulation tool for the description of high-purity Ge detectors and its application to derive the survival probabilities of neutrinoless double decays of ^{76}Ge and of internal decays of ^{68}Ga and ^{60}Co in BEGe type detectors.

The interaction points of the gamma-rays in the crystal are simulated with the GEANT4 based MaGe framework; the pulse shapes associated to the interaction points are determined based on the electric field calculation with an enhanced version of the MGS program. The outputs of the two computations are combined together to determine the final pulse shape corresponding to the interaction of the gamma rays within the detector. This pulse shape is then convoluted with the front-end electronics response and experimentally measured noise to produce signals that can be directly compared to the experimental pulse shapes.

The particular case of the BEGe detector chosen for the specific application of the simulation is related to the future use of this type of detectors in the Phase II of the GERDA neutrino-

less double beta decay experiment. Previous measurements performed with gamma-ray sources have evidenced an enhanced capability of these detectors to discriminate between single-site and multiple-site events from the analysis of the signal pulse shape. The characteristic spread in time of the signal current pulse created by the different charge clusters of a multi-site event has its origin in the sharply rising weighting potential close to the small read-out electrode.

The validation of the simulation was performed in two different ways. In one of them the calculated pulses and their rise times are compared to the measured ones generated in well defined positions by the low-energy gamma rays of an ^{241}Am source. This method is limited to the region near the outer surface of the Ge crystal and strongly affected by the definition of the dead layer and the size of the spatial grid in the calculation. The other is an integral method and involves the comparisons of the rise time and A/E distributions obtained from simulated and experimentally recorded interactions of high-energy gamma-rays from a ^{208}Tl source with the crystal. Such gamma rays interact in the whole volume of the detector and the result of the comparison is a measure of the overall goodness of the simulation. Both methods show a good agreement between the measured and simulated data. The slight deviations are mainly due to inaccuracy in the geometry definition (especially important in case of the p+ electrode), the finite grid width used for defining the library of pulses and the charge carrier mobility model parametrization (measured by using a different crystal at a different temperature).

The simulation was then used to estimate the capability of the pulse shape discrimination method to reduce the gamma-ray background produced by internal ^{68}Ga and ^{60}Co sources in the energy region of the $0\nu\beta\beta$ decay. The ^{76}Ge $0\nu\beta\beta$ decay was also simulated in order to determine the PSD acceptance of its signal. The results are presently dominated by systematic errors related to analysis adjustments developed to overcome the imperfections of the simulation, as the A/E parameter is particularly sensitive to such effects. Nevertheless, the outcome represents a reasonable prediction of the PSD background discrimination efficiency for the GERDA experiment. The $0\nu\beta\beta$ decay acceptance was found to be $(86 \pm 3)\%$, while the internal backgrounds were drastically reduced. Only $(0.9^{+0.4}_{-0.2})\%$ of ^{60}Co events and $(4.5 \pm 0.3)\%$ of ^{68}Ga events at $Q_{\beta\beta}$ remain after the analysis cut. The ^{68}Ga suppression can be combined with the time coincidence rejection method proposed in [4] which takes advantage of the short (1 hour) half life of ^{68}Ga and the 10 keV X-ray or Auger electron emission ($\sim 86\%$ probability) from its mother isotope ^{68}Ge . This latter method, providing reduction by about a factor of 5, will also benefit from the low-noise characteristic of BEGe detectors, maintaining a low-energy threshold well below the interesting 10 keV X-ray energy. Owing to the unique qualities of BEGe detectors, two of the most challenging GERDA backgrounds, originating from internal ^{60}Co and ^{68}Ga produced by cosmic ray interactions in germanium, can be reduced by a factor of 100 by analysis of the germanium signal only.

Acknowledgments

The authors would like to thank Dino Bazzacco, Bernhard Schwingenheuer, Stefano Riboldi and Enrico Borsato for the stimulating discussions and useful comments on this work. They also acknowledge Matthias Laubenstein for providing help and supporting the measurements in the low background laboratory.

This work was supported in part by the Transregio Sonderforschungsbereich SFB/TR27 “Neutrinos and Beyond” by the Deutsche Forschungsgemeinschaft and by the Munich Cluster of Excellence “Origin and Structure of the Universe”.

References

- [1] E. Fiorini, A. Pullia, G. Bertolini, F. Cappellani and G. Restelli, *A search for lepton nonconservation in double beta decay with a germanium detector*, Phys. Lett. B 25 (1967) 602.
- [2] M. Gunther et al *Heidelberg–Moscow experiment with Ge-76: Full setup with five detectors*, Phys. Rev. D 55 (1997) 54.
C. E. Aalseth et al. (IGEX Collaboration), *Recent results of IGEX ^{76}Ge double–beta decay experiment*, Phys. of Atomic Nuclei 63 (2000) 1225.
- [3] H.V. Klapdor-Kleingrothaus, A. Dietz, I.V. Krivosheina and O. Chkvorets, *Data acquisition and analysis of the ^{76}Ge double beta experiment in Gran Sasso 1990–2003*, Nucl. Inst. Meth. A 522 (2004) 371.
- [4] GERDA Collaboration, I. Abt et al., *GERDA: The GERmanium Detector Array for the search of neutrinoless $\beta\beta$ decay of ^{76}Ge at LNGS*, hep-ex/0404039.
- [5] F. Feruglio, A. Strumia and F. Vissani, *Neutrino oscillations and signals in β and $0\nu\beta\beta$ experiments*, Nucl. Phys. B 637 (2002) 345. *First KamLAND results*, Nucl. Phys. B 659 (2003) 359.
- [6] Canberra Semiconductor NV, Lammerdries 25, B–2430 Olen, Belgium.
- [7] D. Budjáš, M. Barnabé Heider, O. Chkvorets, N. Khanbekova and S. Schönert, *Pulse Shape Analysis with a Broad-Energy Germanium Detector for the GERDA experiment*, 2009 JINST 4 P10007.
- [8] D. Budjáš, *Germanium Detector Studies in the Framework of the GERDA experiment*, Dissertation, University of Heidelberg (2009).
- [9] M. Barnabé Heider, D. Budjáš, K. Gusev and S. Schönert, *Operation and performance of a bare broad-energy germanium detector in liquid argon*, 2010 JINST 5 P10007.
- [10] M. Agostini et al., *Procurement, production and testing of BEGe detectors depleted in ^{76}Ge* , to appear in Nucl. Phys. B, Proc. Suppl.(Neutrino 2010).
- [11] Majorana Collaboration, C. E. Aalseth et al., *The Majorana neutrinoless double-beta decay experiment*, Phys. Atom. Nucl. 67 (2004) 2002 [Yad. Fiz. 67 (2004) 2025] [arXiv:hep-ex/0405008].
- [12] P. S. Barbeau, J. I. Collar and O. Tench, *Large-Mass Ultra-Low Noise Germanium Detectors: Performance and Applications in Neutrino and Astroparticle Physics*, JCAP 0709 (2007) 009 [arXiv:nucl-ex/0701012].
- [13] Geant4 Collaboration, S. Agostinelli et al. , *GEANT4: A simulation toolkit*, Nucl. Instrum. and Meth. A 506 (2003) 250.
- [14] J. Allison et al., *GEANT4 developments and applications*, IEEE Trans. Nucl. Sci. 53 (2006) 270.
- [15] M. Bauer et al, *MaGe: a Monte Carlo framework for the Gerda and Majorana double beta decay experiments*, J. Phys.: Conf. Ser. 39 (2006) 362;
M. Boswell et al, *MaGe - a Geant4-based Monte Carlo Application Framework for Low-background Germanium Experiments*, arXiv:1011.3827v1.
- [16] P. Medina, C. Santos and D. Villaume, *A simple method for the characterization of HPGe detectors*, IEEE IMTC (2004).

- [17] L. Mihailescu, W. Gast, R.M. Lieder, H.Brands and H. Jager, *The influence of anisotropic electron drift velocity on the signal shapes of closed-end HPGe detector*, Nucl. Inst. and Meth. A 447 (2000) 350.
- [18] B. Bruyneel, P. Reiter and G. Pascovici, *Characterization of large volume HPGe detectors. Part I: Electron and hole mobility parametrisation*, Nucl. Inst. and Meth. A 569 (2006) 764.
- [19] Zhong He, *Review of the Shockley-Ramo theorem and its application in semiconductor gamma-ray detectors*, Nucl. Inst. and Meth. A 463 (2001) 250.
- [20] CANBERRA Broad Energy Ge (BEGe) Detector, catalogue accessed at URL: <http://www.canberra.com/products/485.asp>.
- [21] M. Agostini, *Characterization of a Broad Energy Germanium detector through advanced pulse shape analysis techniques for the GERDA double-beta decay experiment*, Master Thesis, University of Padova (2009).
- [22] M. Agostini et al., *Study of performances of a Broad Energy germanium detector*, companion paper, submitted to JINST.
- [23] See <http://www.caen.it/nuclear/product.php?mod=N1728B>.
- [24] See <http://www.iphc.cnrs.fr/-TUC-.html>.
- [25] M. Agostini, L. Pandola, P. Zavarise and O. Volynets, *GELATIO: a general framework for modular digital analysis of HPGe signals*, in preparation.
- [26] J. Stein, F. Scheuer, W. Gast and A. Georgiev, *X-ray detectors with digitalizer preamplifiers*, Nucl. Inst. and Meth. B 113 (1996) 141.
- [27] M.G. Strauss and R.N. Larsen, *Pulse height defect due to electron interaction in the dead layers of Ge(li) γ -Ray detectors*, Nucl. Inst. and Meth. 56 (1967) 80.
- [28] C.E. Aalseth et al., *Results from a Search for Light-Mass Dark Matter with a P-type Point Contact Germanium Detector*, arXiv:1002.4703v2.